# Cronfa - Swansea University Open Access Repository

_____

This is an author produced version of a paper published in :
_Renewable Energy_

_____

Cronfa URL for this paper:

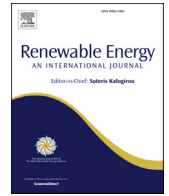http://cronfa.swan.ac.uk/Record/cronfa29491

_____

_____

# An enhanced disk averaged CFD model for the simulation of horizontal axis tidal turbines

CrossMark

M. Edmunds[*], A.J. Williams, I. Masters, T.N. Croft

*Marine Energy Research Group, College of Engineering, Swansea University, Wales, SA2 8PP, UK*

A B S T R A C T

Simulating fully resolved Horizontal Axis Tidal Turbine (HATT) geometry for a time period great enough to resolve a fully developed wake, and accurately predict power and thrust characteristics, is computationally very expensive. The BEM-CFD method is an enhanced actuator disk and is able to reduce the computational cost by simulating a time averaged downstream velocity field. Current implementations fall short of accurately determining tip losses, which are a function of the hydrofoil geometry. This work proposes a method of addressing this shortfall by modifying the angle of attack to conform to the constraints outlined in Prandtl's lifting line theory, i.e. the zero lift angle of attack at the hydrofoil tip. The revised model is compared to existing BEM-CFD methods and validated against experimental data. The revised BEM-CFD method presented in this work shows a significant improvement over previous BEM-CFD methods when predicting power and thrust. The coefficient of power is reduced from 0.57 (approx. 30% above experiment) to 0.44 (approx. 3% above experiment). An increase in turbulence intensity in the rotor region, in particular at the wake boundary, improves the recovery of the wake without the addition of empirical turbulence source terms. Good correlation with experimental results for power, thrust and wake prediction, is observed. The model may also be applied to wind turbines.

© 2016 The Authors. Published by Elsevier Ltd. This is an open access article under the CC BY license (http://creativecommons.org/licenses/by/4.0/).

## 1. Introduction

Tidal stream renewable energy is becoming an increasingly viable source of energy production, as knowledge and technology in this sector develops. Tidal stream power generation has emerged in recent years as a potentially reliable form of renewable energy due to the predictability of tidal periods and magnitudes [1]. While many tidal sites across the world are being identified with economically attractive levels of energy extraction, the UK is of particular interest due to the high concentration of available resource [2]. To meet the growing requirements of this sector, investment in improving current tidal stream power extraction knowledge and technology is necessary. This can be achieved through the study of practical experiment, or numerical and analytical modelling [3—5].

Although laboratory experiments cannot truly mimic complex offshore conditions, they are very convenient due to significantly lower costs compared to offshore deployments. Laboratory

experiments provide a platform for collecting accurate and repeatable data. In contrast, Computational Fluid Dynamics (CFD) modelling has the potential to simulate the effect on environmental conditions at significantly lower cost compared to offshore deployments.

To address this a number of Blade Element Momentum Theory (BEMT) techniques, originally derived from Glauert's propeller theory [6], have been introduced. BEMT [6,7] is an analytical approach which uses tabulated aerofoil data to perform analysis. This technique is extensively used in the wind industry due to the simplicity of the model, and the agreement of its results with measured data [8]. The BEMT model has also successfully been applied to Horizontal Axis Tidal Turbines (HATTs). A typical HATT may see several complex flow scenarios throughout its operational range and therefore, a number of empirical corrections have been developed to better correlate the BEMT model with experimental results [9]. These include corrections for yawed rotors, hub losses, tip losses, and heavily loaded rotors.

A significant limitation of the BEMT method is the inability to simulate the local velocity field, and thus perform analysis on the downstream wake characteristics. Where this is required, alternative modelling methods need to be employed. One alternative is the

* Corresponding author.
E-mail address: m.edmunds@swansea.ac.uk (M. Edmunds).

transient CFD simulation of a HATT with fully resolved hydrofoil geometry. However simulating fully resolved HATT geometry for a time period great enough to resolve a fully developed wake, and accurately predict power and thrust characteristics [10], is computationally very expensive [11].

An alternative to the transient fully resolved geometry of a HATT is the steady state, or time averaged, Blade Element Momentum CFD (BEM-CFD) computational model [12–14]. This model combines elements of BEMT with CFD simulation techniques to resolves the hydrofoil's effect on the flow in a steady state simulation. This technique significantly reduces the computational cost of simulating HATTs. The advantage of the BEM-CFD method is the prediction of a time averaged downstream velocity field, in particular the downstream wake.

Although the current BEM-CFD methods can predict the power and thrust available at the turbine, recent comparisons with experimental data [15,16] highlight the need for further investigation into the accuracy of this type of model. Of particular interest is the assumption that correction factors applied to the BEMT analytical model, as discussed in Ref. [9], are directly transferable to the BEM-CFD numerical model.

In the case of a three dimensional finite hydrofoil geometry, pressure differences between the upper and lower surfaces induce flow spillage at the tip. In turn this motion generates the tip vortices as described in Ref. [6]. This spillage has a knock on effect across the full span of the hydrofoil, and thus reduces its efficiency with the greatest losses towards the tip. The BEM-CFD model averages the effect of a hydrofoil over a complete rotation, therefore there is no upper and lower surface to propagate the flow resulting from a pressure difference. In Ref. [16] the authors reasoned similarly and thus added the Prandtl tip loss factor to the momentum source terms of the BEM-CFD model. They then compared the power and thrust coefficients to experimental results published in Ref. [17].

In classical BEMT implementation the model correction factors are applied directly to the axial and tangential induction factors, as demonstrated by Ref. [9]. From this the forces acting on the hydrofoil are computed. In the case of the Prandtl tip loss factor, the effective force on the hydrofoil is reduced towards the tip. If this is applied to BEM-CFD in the same way, as in Ref. [16], the effect of the hydrofoil on the flow is reduced. If the annular stream tubes close to the tip are considered in detail, the implementation of a tip loss as reduction in reactive force from the hydrofoil allows the fluid to pass the hydrofoil with little momentum change. Although this is not an issue for BEMT as the velocity field is not simulated, this is a significant issue for the BEM-CFD method as accurate results are dependant on the correct flow characteristics in this area.

To address these challenges, this work introduces and investigates the effectiveness of a revised BEM-CFD model based on elements of Prandtl's analytical lifting line theory as defined in Ref. [6]. This work proposes modifying the angle of attack, and thus the distribution of downwash across the hydrofoil, as a result of the tip constraints outlined in Prandtl's lifting line theory, i.e. the zero lift angle of attack at the hydrofoil tip. The revised model is compared to existing BEM-CFD methods and validated against experimental data. The revised BEM-CFD method presented in this work shows a significant improvement over previous BEM-CFD methods when predicting power and thrust. This approach deals appropriately with the tip losses encountered with a hydrofoil of finite length, and significantly improves the formation of the local velocity field. The revised BEM-CFD model is compared to; the classical BEMT method, the BEM-CFD with Prandtl tip loss applied directly to the momentum source terms, and experimental data.

This paper introduces the revised model in Section 2, defines a case study in Section 3, discusses the comparative results in Section 3.4, forms conclusions in Section 4, and finally highlights the

potential future work in Section 5.

## 2. The numerical model

This section introduces the revised numerical model for predicting the performance of HATTs (Horizontal Axis Tidal Turbines). The model is a hybrid analytical, BEM, and CFD computational model. First is a short discussion of the CFD process, governing equations and turbulence models (Section 2.1). The following section revisits the standard BEM-CFD approach (Section 2.2), as described by Ref. [14]. Following this a description of the revised model for improving the prediction of potential power and thrust generation (Section 2.3) is provided.

### 2.1. CFD and the governing equations

CFD simulations are conducted using Physica, a framework for multi-physics Computational Fluid Dynamics and Computational Solid Mechanics [18]. Linking the CFD flow domain to the BEM model is achieved by additional source terms included within the conservation of momentum equations of the Physica finite volume solver. The solver uses steady state Reynolds averaged incompressible Navier-Stokes equations with a range of turbulence model options including K-Epsilon, K-Epsilon RNG, and K-Omega. Physica has been developed by Ref. [19]. An alternate implementation has also been developed in OpenFOAM [20].

The CFD model requires the solution of the Navier Stokes equations representing the conservation of mass and momentum. These equations are expressed as follows:

$$\nabla \cdot (\rho \overrightarrow{v}) = 0 \qquad (1)$$

$$\nabla \cdot (\rho \overrightarrow{v} v_i) = -\frac{\partial p}{\partial x_i} + \nabla \cdot ([\mu_l + \mu_t] \nabla v_i) + S_i \qquad (2)$$

where $\rho$ is the density, $\overrightarrow{v}$ is the velocity vector, $v_i$ is the $i$th component of the velocity vector, $\mu_l$ and $\mu_t$ are the laminar and turbulent dynamic viscosities respectively, and $S_i$ includes an additional source representing the moving rotor.

A widely used method for simulating the effect of turbulence on the mean flow, at the sub grid level, is the $k$-$\varepsilon$ turbulence model [21]. Although this model is relatively simple, stable, and requires modest computational cost, it is limited by the single length scale used to calculate the viscous properties of the turbulent fluctuations. Diffusion, as a result of the turbulent fluctuations, does not occur at just one length scale. The $k$-$\varepsilon$ RNG model [22] tries to address this issue by utilising statistical analysis to describe the set of turbulent length scales. Although these models regard turbulence as being isotropic in nature, in rotational flow, such as found in turbine wakes, the turbulent eddies are likely anisotropic. Higher order models, which include the Reynolds stress model or large eddy simulation, can better predict the turbulent flow characteristics. These models, however, require greater computational expense.

In this work the focus on performance of turbine rotors, rather than flow structures of the highly turbulent near wake region immediately downstream of the device, justifies the use of the $k$-$\varepsilon$ RNG model. In this model two equations are solved; $k$ represents the energy contained within the turbulent fluctuations, and $\varepsilon$ represents the dissipation rate of this energy. The equations for the transport of these variables are similar in form to the momentum equations:

$$\nabla \cdot (\rho \vec{v} k) = \nabla \cdot \left( \left[ \mu_l + \frac{\mu_t}{\sigma_k} \right] \nabla k \right) + \mu_t G - \rho \varepsilon \qquad (3)$$

$$\nabla \cdot (\rho \vec{v} \varepsilon) = \nabla \cdot \left( \left[ \mu_l + \frac{\mu_t}{\sigma_\varepsilon} \right] \nabla \varepsilon \right) + C_{1\varepsilon} \mu_t G \frac{\varepsilon}{k} - C_{2\varepsilon} \left( \frac{C_\mu \eta^3 [1 - \eta/\eta_0]}{1 + \beta \eta^3} \right) \qquad (4)$$

where:

$$\eta = \sqrt{G} \, \frac{k}{\varepsilon} \qquad (5)$$

These equations are used to calculate a turbulent viscosity:

$$\mu_t = \frac{\rho C_\mu k^2}{\varepsilon} \qquad (6)$$

In Equations (3), (4) and (6); $\sigma_k$, $\sigma_\varepsilon$, $C_{1\varepsilon}$, $C_{2\varepsilon}$, $C_\mu$, $\beta$, and $\eta_0$ are taken to be constants, and $G$ represents the turbulent generation rate. The viscosity components of the $k$ and $\varepsilon$ equation diffusion terms, are effectively the sum of the laminar and turbulent viscosities.

## 2.2. The BEM-CFD method

Fluid flowing over the surface of a body has a force exerted on it. Of interest, when describing hydrofoils, are the lift and drag components of this force, see Fig. 1. Lift is defined as a force perpendicular to the free stream flow direction. Drag is defined as being parallel to, and opposing, the free stream flow direction. These hydrodynamic forces can be described by the following equations:

$$F_L = 0.5 \rho \vec{v}^2 A C_L \qquad (7)$$

$$F_D = 0.5 \rho \vec{v}^2 A C_D \qquad (8)$$

where $F_L$ is lift force, and $F_D$ is drag force, $\rho$ is fluid density, $\vec{v}$ is velocity, $A$ is area, $C_L$ is the coefficient of lift, and $C_D$ is the coefficient of drag. The coefficients of lift and drag are dependant on the angle of attack, $\alpha$, the geometric properties of the hydrofoil, and the Reynolds Number. Data for a wide range of profiles is available from a number of sources including [23]. The chord and twist geometric properties, in combination with the profile $C_L$ and $C_D$ characteristics, are a function of the overall rotor design/performance requirements.

The influence of a tidal turbine with multiple hydrofoils (or blades) is averaged over a rotational interval, i.e. the rotor applies the same force to all locations at the same radial distance from the rotor centre on a given axial plane. The magnitude of these forces are a function of the hydrofoil geometry, its hydrodynamic properties, the quantity of hydrofoils, and their speed relative to the flow.

The BEM-CFD model is formulated such that the relevant characteristics of the hydrofoil are introduced through additional source terms appended to the momentum equation, see Section 2.1. Due to the Reynolds averaged nature of the solution, transient flow features caused by the hydrofoil position fail to be resolved. These include tip vortices, the laminar to turbulent transition across the hydrofoil surface, flow separation, and turbulence generation along the downstream part of the hydrofoil.

Fig. 1 shows how a turbine with three hydrofoils is discretised for use with the blade element method. The hydrofoil properties are determined at radius $r_i$, and then averaged over $2\pi$ radians. This process is repeated for each hydrofoil element over the interval $[r_0, r_{max}]$.

The fluid applies axial and tangential forces to each element as illustrated in Fig. 1. Here $F_T$ is the tangential force and $F_A$ represents the axial force. The lift and drag forces, $F_L$ and $F_D$ respectively, are dependent on the effective angle of attack $\alpha_e$. This is the angle between the hydrofoil element and the resultant velocity $\vec{v}_r$.

Based on the approach in Ref. [7], an axial force on a hydrofoil can be defined as follows:

$$F_A = F_L sin\phi + F_D cos\phi \qquad (9)$$

and the tangential force on a hydrofoil can be defined as:

$$F_T = F_L cos\phi - F_D sin\phi \qquad (10)$$

where $\phi$ is the flow inclination angle defined by:

$$\phi = tan^{-1}((\omega r - v_t)/v_a) \qquad (11)$$

Here $v_t$ and $v_a$ are the tangential and axial velocities respectively, and $\omega$ is angular velocity [$rad/s$]. The variation in lift force $dF_L$, and drag force $dF_D$, acting along the hydrofoil radius are given as follows:
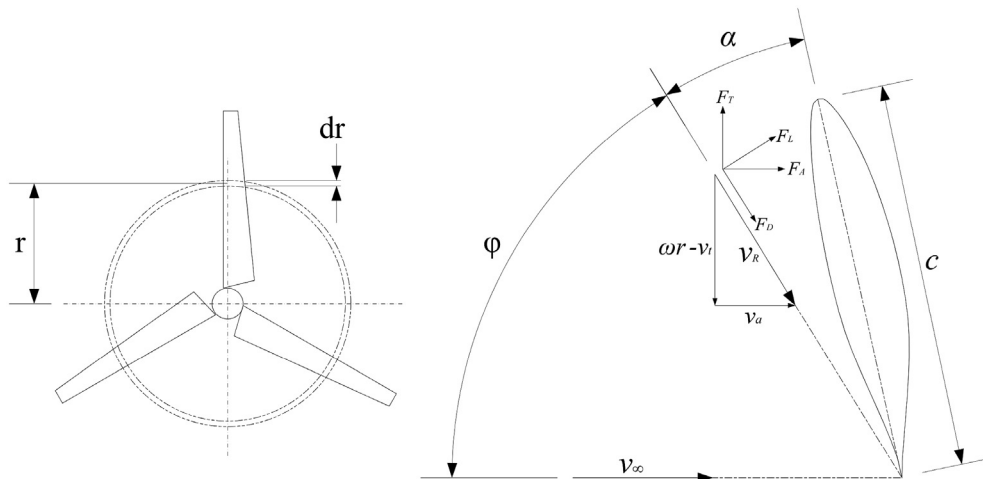


**Fig. 1.** Blade element method rotor discretisation scheme.

$$dF_L = 0.5\rho \left| \overrightarrow{v}_r \right|^2 C_L c dr \tag{12}$$

$$dF_D = 0.5\rho \left| \overrightarrow{v}_r \right|^2 C_D c dr \tag{13}$$

where $C_L$ and $C_D$ are the lift and drag coefficients respectively, $c$ is the chord length, and:

$$\left| \overrightarrow{v}_r \right|^2 = v_a^2 + (\omega r - v_t)^2 \tag{14}$$

Substituting Equations (12) and (13) into Equations (9) and (10) gives the following:

$$\begin{aligned} S_a &= dF_A \\ &= 0.5\rho \left| \overrightarrow{v}_r \right|^2 c dr (C_L \sin\phi + C_D \cos\phi) \end{aligned} \tag{15}$$

$$\begin{aligned} S_t &= dF_T \\ &= 0.5\rho \left| \overrightarrow{v}_r \right|^2 c dr (C_L \cos\phi - C_D \sin\phi) \end{aligned} \tag{16}$$

which, when resolved to Cartesian components and converted to force per volume, are combined with the momentum equation (Section 2.1 Equation (2)) as the source term $S_i$.

## 2.3. The analytical augmentation of BEM-CFD

In Section 2.2 it is noted that the flow features associated with a transient CFD simulation of fully resolved hydrofoil geometry, are not present in a steady state BEM-CFD simulation. One particular characteristic of interest is the vortex generated at the hydrofoil tip. The vortex is the result of pressure differentials between the upper and lower surfaces of the hydrofoil. The difference in pressure encourages flow to pass from the lower surface to the upper around the hydrofoil tip. This motion, combined with the oncoming free stream flow, generates the trailing tip vortex.

The trailing vortex structures emanating from the tip of the hydrofoil have a negative impact on overall lift efficiency. This is due to the velocity direction not remaining planar to the hydrofoil profile, i.e. it is propagating towards the tip. Another observed effect is the change in angle of attack relative to an idealised infinitely long 2D hydrofoil. Ref. [6] states that the angle of attack is reduced to the zero lift condition at the tip of a wing (or hydrofoil), and also describes the distribution of this change in angle of attack along the length of a wing (or hydrofoil). This section starts with a summary of the analytical approach for estimating this effect, and then follows with a description of the revised model for capturing the effect of efficiency loss due to the generation of trailing tip vortices.

### 2.3.1. Downwash, induced angle of attack, and Prandtl's classical lifting line theory

The field of aerodynamics describes the lift force on a wing as the result of a pressure differential between the lower and upper wing surfaces. The associated difference in flow speed above and below the wing section can be characterised as circulation (or vorticity). The net effect of the induced circulation is to deflect the airflow in a downward direction. This downward deflection is known as *downwash*.

Circulation theory, see Ref. [24], states that the lift force of a wing of constant section and unit span is calculated thus:

$$F_L = \rho_\infty v_\infty \Gamma \tag{17}$$

where $\rho_\infty$ is free stream density, $v_\infty$ is free stream velocity magnitude, and $\Gamma$ is circulation. The downward velocity induced by the circulation is defined as:

$$w = \Gamma / (2\pi h) \tag{18}$$

where $w$ is the downwash velocity magnitude at a given distance $h$ from the centre of vorticity rotation.

Fig. 2 shows the geometric angle of attack $\alpha$ is made up of two components. The induced angle of attack, $\alpha_i$, quantifies the angle of downward deflection as a result of the induced downwash. The induced angle of attack can be computed thus:

$$\alpha_i = \tan^{-1} w / v_\infty \tag{19}$$

The following relationship defines the effective angle of attack $\alpha_e$:

$$\alpha_e = \alpha - \alpha_i \tag{20}$$

The subject of wing tip vortices is described by Refs. [6,24]. The vortices are essentially weak tornadoes that trail downstream of the finite wing. These wing tip vortices downstream of the wing induce an additional small downward component of air velocity in the neighbourhood of the wing itself. This additional downward component, or additional downwash, varies across the full span of a finite wing. Prandtl's classical lifting line theory, as detailed in Ref. [6], describes this phenomena in terms of an infinite number of horseshoe vortices distributed across the wing span, compounded towards the root of the span. This gives rise to the notion of a trailing vortex sheet.

The spanwise component of the velocity vector on the upper surface is directed from tip to hub, and the opposite direction (from the hub to tip) on the lower surface. The physical effect of the resultant shear at the trailing edge is the development of a trailing vortex sheet that contains vorticity. The theory states that for a finite wing, $\alpha_e$ at the wing tip is constrained as the angle of attack at which $F_L = 0$, or $\alpha_{F_L=0}$. This then influences the distribution of downwash across the span. The theory demonstrates methods for calculating the span wise distribution based on the geometric properties of the wing. Ref. [24] discusses a generalised elliptical distribution, derived from an elliptical wing planform, that is a reasonable approximation for the commonly used tapered wing planform. In summary, the distribution of vortex induced downwash takes an elliptical form from root to tip, with the tip constraint of $\alpha_{F_L=0}$.

### 2.3.2. Application of lifting line theory to BEM-CFD

From Equation (11) the flow inclination angle is computed relative to the free stream flow direction, which when subtracted from the hydrofoil twist angle gives the effective angle of attack, see Figs. 1 and 2. The tangential component of this equation includes both the geometric ($\omega r$) and deflection ($v_t$) quantities. Here $\omega r$ is the rotational velocity at the given radius and calculated from the Tip Speed Ratio (TSR) [8] of the rotor, and $v_t$ is the tangential velocity of the deflection relative to the free stream velocity direction, which is solved numerically. The angle between these two components is known as the induced angle of attack $\alpha_i$ or downwash angle, see Fig. 2. However the current BEM-CFD model, due to the steady state disc averaged nature of the method, considers the hydrofoil representation as an infinite two dimensional representation. Thus the additional downwash induced by the presence of tip vortices is not captured.

The BEMT method for predicting turbines encapsulates this same phenomena with the tangential induction factor (commonly represented by $a'$ or $b$). The tangential induction factor represents the deflection (or downwash) of the flow. With the BEMT theory,
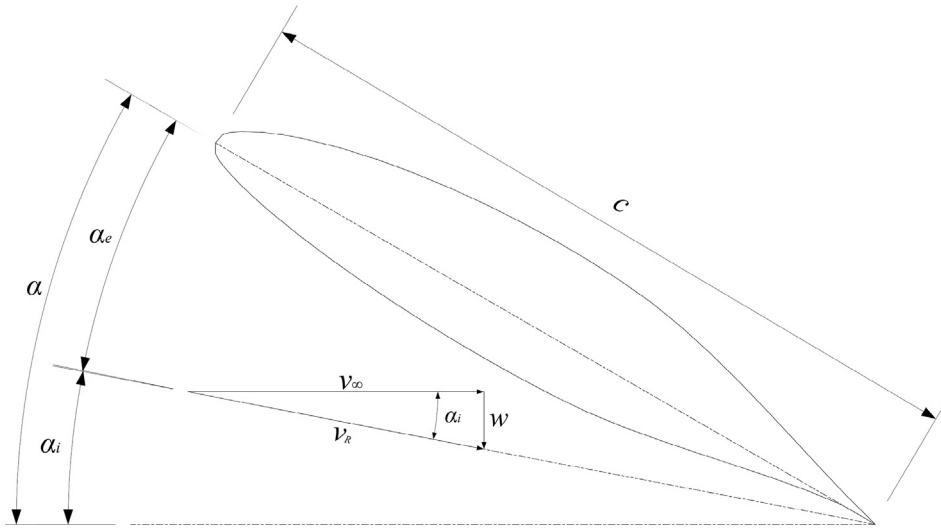
**Fig. 2.** This diagram highlights the components required to define the induced angle of attack $\alpha_i$.

the tip losses associated with the tip vortices are corrected with the use of the Prandtl tip loss factor, see Refs. [9,16]. The tip loss factor is applied to the induction factors effectively reducing the transfer of force to the hydrofoil towards the tip. This method works well for BEMT as the velocity field itself is not computed. However for BEM-CFD, reducing the transfer of momentum from the fluid to the hydrofoil also reduces the deflection of the flow towards the tip of the hydrofoil. This scenario is not a good fit for the established effect on the flow field in this region, and thus produces a poor correction to the current BEM-CFD model to account for tip losses. The effect of the Prandtl tip loss correction applied to BEM-CFD, is very well described in the work by Ref. [16].

To better account for the effect of tip vortices on the flow field, Prandtl's classical lifting line theory is drawn upon to compute an additional source term which represents the additional downwash caused by the tip vortices. This is achieved by computing the additional downwash velocity, $\vec{w}_a$, required to change the currently computed $\alpha_e$ to equal $\alpha_{F_L=0}$. The influence of $\vec{w}_a$ is then weighted by the elliptical distribution function $E(r)$. $E(r) \in [0,...,1]$ is an elliptical function which returns a value between zero (at the tip) and one (at the root) for a given radius $r$ (or span wise distance from the root). The resultant downwash velocity is then used to compute an additional reactive force:

$$S_v = dF_v$$
$$= 0.5\rho \left| \vec{w}_a \right|^2 cdr \tag{21}$$

where $dF_v$ is the additional downwash force required to achieve the flow deflection so that $\vec{w}_a$ is correct at the trailing edge. This is implemented through $S_v$, the additional source term which, when resolved to Cartesian components and converted to force per volume, is combined with the momentum equation (Section 2.1), as an addition to the source term $S_i$.

The source term $S_i$ is a three tuple representing the change in kinetic energy per unit volume (or dynamic pressure) in Cartesian space i.e. $-p/x_i$ in Cartesian coordinates [18]. The scalar terms $S_a$ and $S_t$ are the magnitudes of kinetic energy per unit volume in the axial and tangential directions. In addition the source term $S_v$ represents the additional downwash force. The source term $S_i$ is computed thus:

$$S_i = S_a \widehat{v_a}_i + S_t \widehat{v_t}_i + S_v \widehat{v_w}_i \tag{22}$$

where $\widehat{v_a}$ is the axial unit vector, $\widehat{v_t}$ is the tangential unit vector, and $\widehat{v_w}$ is the unit vector normal to $\alpha_{F_L=0}$, residing on the plane defined by $\widehat{v_a}$ and $\widehat{v_t}$.

The application of this method is restricted to horizontal axis tidal turbines with open ended hydrofoils, i.e. a turbine design which does not incorporate an outer ring, or ducting. The elliptical lift distribution is an approximation for tapered hydrofoils, thus use of this method on hydrofoils which move away from the tapered concept are likely subject to increased simulation error. The important points to consider when using this method is the determination of the correct angle of attack at zero lift condition for the desired hydrofoil geometry, and correctly determined Reynolds numbers and related lift and drag coefficients to better represent the hydrofoils.

### 2.4. Power, thrust, and turbulence measures

This subsection describes the power coefficient $C_P$, thrust coefficient $C_T$ and turbulence intensity $Ti$ measures used in the remainder of this work. The rotor assembly thrust correction computation, used to correct the experimental assembly thrust data, is also defined here.

#### 2.4.1. Power coefficient

The power coefficient $C_P$ is defined as the ratio of power extracted by the rotor hydrofoils, and the maximum available power from flow. To obtain a representative assessment of the incoming flow to the turbine, the flow region is sampled two diameters upstream. The area used to find the average velocity at this location is equivalent to the swept area of the rotor. This technique captures any velocity gradients which may be present in the water column. The power coefficient is represented by:

$$C_P = \frac{P}{0.5\rho \left| \vec{v} \right|^3 A} \tag{23}$$

where $A$ is the area of the incoming flow, $\left| \vec{v} \right|$ is the disk averaged velocity magnitude sampled two diameters upstream of the rotor, and $P$ is power defined as:

$$P = \int_0^R \omega dT_q \tag{24}$$

Here $\omega$ is angular velocity, and $T_q$ is torque defined as:

$$T_q = \int_0^R r dF_T \tag{25}$$

where $r$ is radius, and $F_T$ is tangential force.

### 2.4.2. Thrust coefficient

The thrust coefficient $C_T$ is defined as the axial force acting upon the turbine as compared to the kinetic energy of the incoming flow. This can be represented by:

$$C_T = \frac{F_A}{0.5\rho \left| \vec{v} \right|^2 A} \tag{26}$$

where $F_A$ is axial force.

### 2.4.3. Thrust correction computation

The thrust force measured in the experimental results [25] actually includes the axial force on the whole structure, i.e. the hydrofoils, the nacelle, and the mast. However, Equation (9) only considers the thrust on the hydrofoils. To correct for this an approximation of the thrust force is calculated, and then added to $T_h$. This revised value can then be used to calculate an approximation of the experimental thrust coefficient $C_{T_e}$:

$$C_{T_e} = \frac{F_A + F_m}{0.5\rho \left| \vec{v} \right|^2 A} \tag{27}$$

where $F_m$ is the nacelle and mast axial force, and $F_A + F_m$ is the total axial force acting on the complete rotor assembly. $F_m$ is the simple addition of drag forces where the mast is represented as a cylinder with $C_D = 1.17$ and the nacelle represented as a bullet with $C_D = 0.295$.

### 2.4.4. Turbulence measures

The turbulence in the experimental study by Ref. [25] is characterised by the use of the turbulence intensity measure. Turbulence intensity ($Ti$) is the ratio of root mean square turbulent velocity fluctuations over the mean velocity:

$$Ti = \frac{\left| \vec{v} \right|'}{\left| \vec{v} \right|} \tag{28}$$

where $\left| \vec{v} \right|$ is the mean velocity, and $\left| \vec{v} \right|'$ is the root mean square turbulent velocity fluctuations:

$$\left| \vec{v} \right|' = \sqrt{\frac{2}{3}k} \tag{29}$$

where $k$ is the turbulent kinetic energy.

## 3. Case study: IFREMER tidal turbine experiments

Studies by Refs. [17,26] evaluate the performance of tidal turbines, while investigations by Refs. [9,14–16,27] validate numerical or analytical models with experimental results. The work by Ref. [25] is of particular interest for the validation of the revised BEM-CFD model.

In this research the experimental work of [25] for a single tidal turbine is compared with various implementations of BEM-CFD. In the following subsections the computational domain and boundary conditions are described, and a mesh sensitivity study is presented. In the results subsection comparisons of; the original BEM-CFD model, the BEM-CFD model with Prandtl tip loss factor, the revised BEM-CFD model described in Section 2, the BEMT model presented by Ref. [9], and the Ref. [25] experimental results, are evaluated with respect to performance and near wake characteristics.

### 3.1. Geometries

The geometry of the flume is represented using a cuboid computational domain. The domain is 18 m in length (x-axis), and represents the main section of the flume, as illustrated in Fig. 3. The domain depth is 2 m (z-axis), while the width is 4 m (y-axis), as illustrated in Fig. 4. The rotor is located in the centre of this domain (location 0,0,0), with the nacelle trailing downstream, as illustrated in Fig. 5.

Figs. 5 and 3 show the layout of the nacelle and the blade box area which is utilised by the BEM-CFD code. The blade box represents a rotor of 0.7 m in diameter, with the thickness of the blade box fixed at 0.04 m. Comparative work considering the inclusion vs. exclusion of a mast structure within the flow is studied in Ref. [28]. With this in mind, and due to the increase in mesh complexity and computational cost, this feature has not been included in the model.

### 3.2. Boundary conditions

In all the test cases presented in this paper a plug flow inlet velocity condition of 0.8 m/s or 1.2 m/s in the x-axis direction is imposed; this best reflects the inflow condition of the experiment in Ref. [25]. A reference pressure of 0 Pa is imposed on the outflow boundary. The dynamic pressure field is calculated relative to this condition. No-slip boundary conditions are applied to the turbine nacelle, to the base, and to the side walls of the channel. An initial wall cell height of 0.005 m provides a non-dimensional wall distance for a wall-bounded flow, i.e. $y^+$, of 100 and 125 for velocities of 1.2 m/s and 0.8 m/s respectively. An initial wall cell height of 0.002 for the nacelle provides a $y^+$ of 73. The boundary layers are fully developed within 2 m of the inlet and are propagated downstream. A symmetry boundary condition is imposed at the top of the domain, simulating open water conditions. In the mesh independence studies the turbine is operating close to an optimal design TSR of 4.5 based on the local velocity at the rotor.

### 3.3. Mesh sensitivity study

The sensitivity of results relative to change in mesh density is an important study. From a computational cost point of view, a reduction in the density of the mesh improves the computational cost and thus time. Conversely, an increase in density can assure mesh independent results particularly in regions of complex flow behaviour. The use of a coupled BEM-CFD model requires a region to be defined in the mesh that is detailed enough to support representation of time averaged rotor characteristics. The downstream wake structure is also complex in nature, and thus needs to be treated similarly.

For this case study the required mesh structures are generated utilising blocking techniques. To achieve the required densities through the domain, and adequately capture the rotor and wake region, the domain is divided into a set of subdomains labelled A to
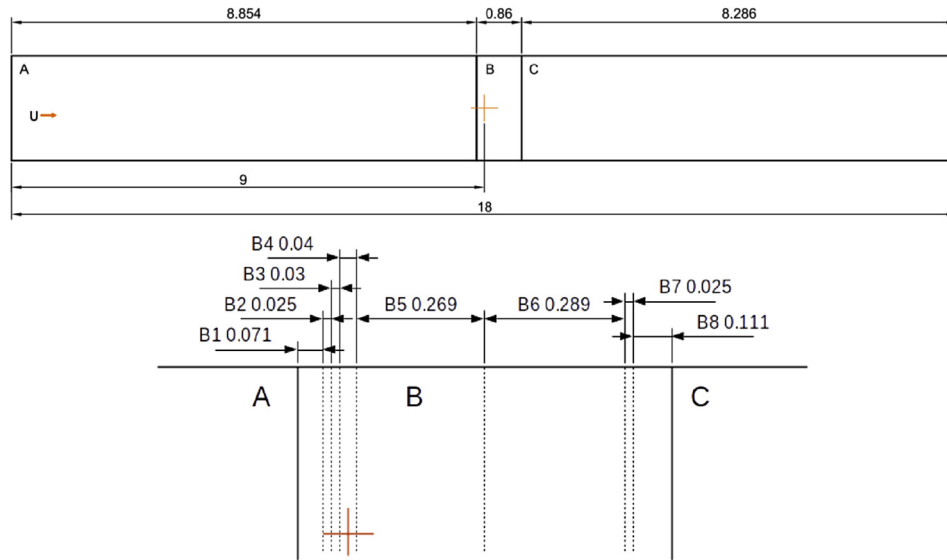
**Fig. 3.** This figure highlights the zones of different mesh densities specified in the x direction. Three zones are shown where; zone A is upstream, B is the bladebox zone, and C is downstream. Zone B is further subdivided into 8 subzones [B1, …,B8] identified in the lower schematic.
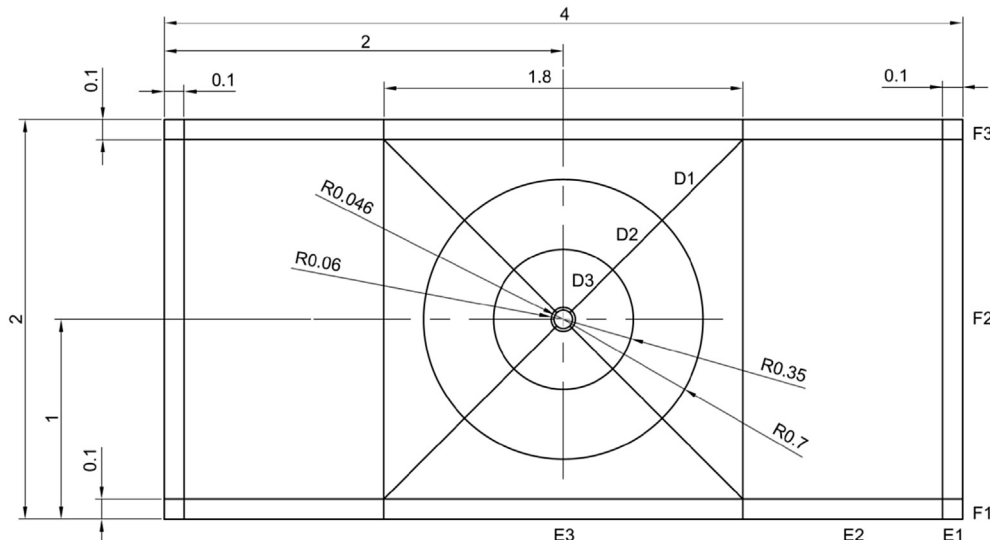


**Fig. 4.** This image shows the inflow boundary of the single turbine domain. The central area is formed from an O-Grid constrained by radial curves which provide control for differing densities at different radii.

C, as illustrated in Fig. 3. The subdomain labelled B is further subdivided, and labelled B1 to B8. An O-grid structure is then defined, which runs the length of the domain capturing the rotor, and approximating the area of the wake, as illustrated in Fig. 4.

Densities are defined for each of the zones, A to C, with reference to the x-axis. The y-axis and z-axis densities are a function of the O-grid parameters, as illustrated in Fig. 4. Table 1 defines the range of densities for each of the zones along the x-axis, the parameters for the O-grid, and the number of elements contained within each of the mesh definitions.

The first attributes of interest are the coefficients with respect to the rotor operation and power extraction. The coefficients of power $C_P$ and axial thrust $C_T$ are measures of the efficiency of power extraction from the water. Definitions for these terms are presented in Section 2.4. Stabilisation or convergence of the coefficients occurs at approximately 3000 iterations. It can be seen in Fig. 6 that the coefficients tend to stabilise around mesh density number 2, and remain consistent thereafter.

The velocity variation resulting from changes in mesh density is the next attribute considered. Fig. 6 illustrates velocities at seven locations within the domain. These locations are detailed in Table 2. The velocity field resolves from approximately 18,000 iterations for mesh number 1 to 25,000 iterations for mesh number 5. The velocities at the specified locations can be seen to stabilise around mesh density number 3, and then remain consistent.

The results of the mesh independence study demonstrate mesh independent results for the velocity field from mesh 3 onwards. However, for accurate representation of the rotor coefficients, independence is reached from mesh 2 onwards. From this study the parameters of mesh 3 produce results which are considered reliably independent. Therefore, the results presented in Section 3.4 have been obtained using mesh 3.
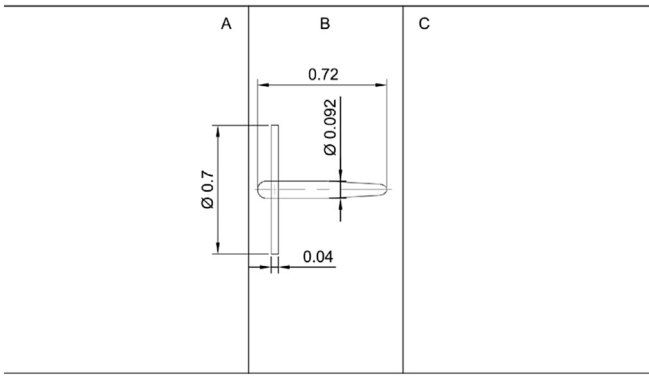
**Fig. 5.** This schematic shows a side view of the rotor configuration. The nacelle is geometrically modelled whereas the blade area (subzone B4 in Fig. 3) is constrained with a dense mesh to support the BEM-CFD model.

measured at the rotor centre (with rotor removed). These results are labelled 'Experiment' in Fig. 7.

The BEMT technique is extensively used in industry in part due to the agreement of its results with measured data. The BEMT implementation described in Ref. [9] is used to create comparative data for this study. When comparing the BEMT method to experiment we can see a strong correlation with $C_P$. The under prediction observed by this method is a result of the blockage effect not simulated with the BEMT approach. The blockage effect, caused by the finite dimensions of the flume cross section, has the consequence of forcing additional flow through the rotor thus artificially raising performance. The blockage ratio for this study is approximately 4.8%. An interesting observation of this comparison, is the smaller than expected difference the blockage effect has in this case study.

In contrast to the BEMT results, the original BEM-CFD method

**Table 1**
This table defines the number of elements in the x-axis direction for zones A to C, as defined in Fig. 3, and the number of elements along the edges D1 to F3, as defined in Fig. 4. For each mesh the total quantity of elements is included.

| Mesh no. | A | B1 | B2 | B3 | B4 | B5 | B6 | B7 | B8 | C | D1 | D2 | D3 | E1 | E2 | E3 | F1 | F2 | F3 | Qty. Elements |
|---|---|---|---|---|---|---|---|---|---|---|---|---|---|---|---|---|---|---|---|---|
| 1 | 80 | 6 | 9 | 3 | 8 | 33 | 33 | 5 | 19 | 191 | 11 | 13 | 23 | 2 | 8 | 14 | 2 | 14 | 1 | 1,258,764 |
| 2 | 90 | 7 | 10 | 4 | 9 | 37 | 37 | 6 | 21 | 215 | 12 | 14 | 25 | 3 | 9 | 16 | 3 | 16 | 1 | 1,805,715 |
| 3 | 100 | 8 | 11 | 5 | 10 | 41 | 41 | 7 | 23 | 239 | 13 | 15 | 27 | 4 | 10 | 18 | 4 | 18 | 1 | 2,418,624 |
| 4 | 110 | 9 | 12 | 6 | 11 | 45 | 45 | 8 | 25 | 243 | 14 | 16 | 29 | 5 | 11 | 20 | 5 | 20 | 1 | 3,987,176 |
| 5 | 120 | 10 | 13 | 7 | 12 | 49 | 49 | 9 | 27 | 287 | 15 | 17 | 31 | 6 | 12 | 22 | 6 | 22 | 1 | 5,153,080 |
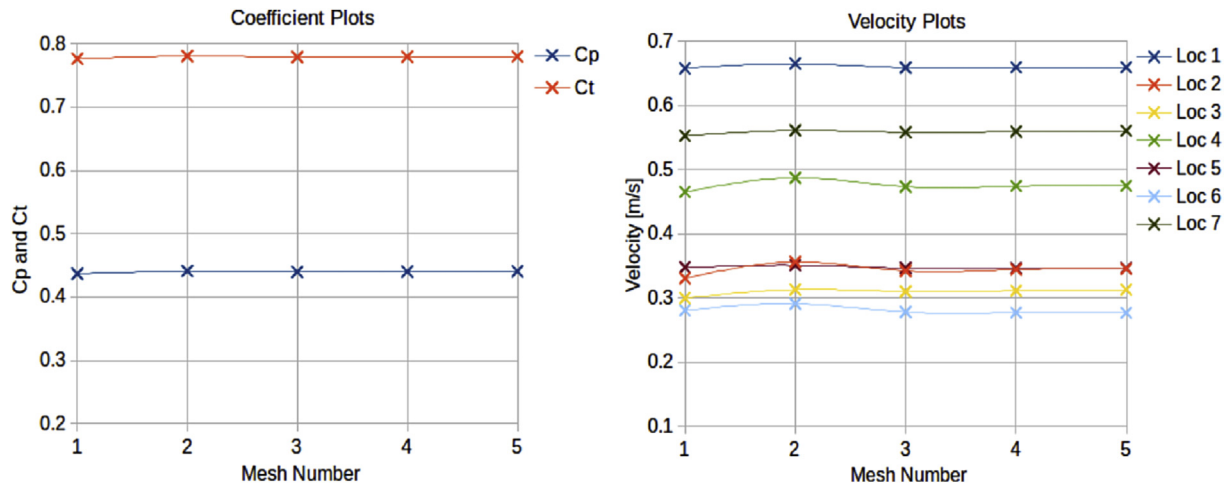


**Fig. 6.** Coefficients of power and thrust plotted against mesh number from coarsest to finest. Velocity at a number of locations specified in Table 2, plotted against mesh number from coarsest to finest.

**Table 2**
This table defines the location of the samples used for the mesh study.

| Axis | Loc 1 | Loc 2 | Loc 3 | Loc 4 | Loc 5 | Loc 6 | Loc 7 |
|---|---|---|---|---|---|---|---|
| x | 0.0 | 8.5 | 2.0 | 5.0 | 0.3 | 3.5 | 0.4 |
| y | 0.075 | 0.0 | 0.0 | 0.3 | 0.3 | 0.0 | 0.075 |
| z | 0.0 | 0.0 | 0.0 | 0.0 | 0.0 | 0.0 | 0.0 |

### 3.4. Results

#### 3.4.1. Comparison of predicted $C_P$ and $C_T$ with experiment

The $C_P$ and $C_T$ results used as the benchmark for this study [25] are taken at a flow speed of 1.2 m/s, with a background Ti of 3%,

used in Ref. [14] shows a significant over prediction of $C_P$ above TSR 2.5. These results are supported with comparative work by Ref. [15] who see similar trends with a standard BEM-CFD model. The BEM-CFD model using the Prandtl tip loss factor, as implemented in Ref. [16], shows a general reduction in prediction of $C_P$ compared to the original BEM-CFD model. However, the trends observed are not in line with the experimental results indicating that it may not be appropriate to use the Prandtl tip loss factor with the BEM-CFD method. The results obtained using the revised BEM-CFD method (as described in Section 2) are also presented in Fig. 7. A close correlation between predicted and experimental values for $C_P$ is observed for this method.

It is observed that the predictions of $C_T$ obtained from the different models, are lower than the experimental values,
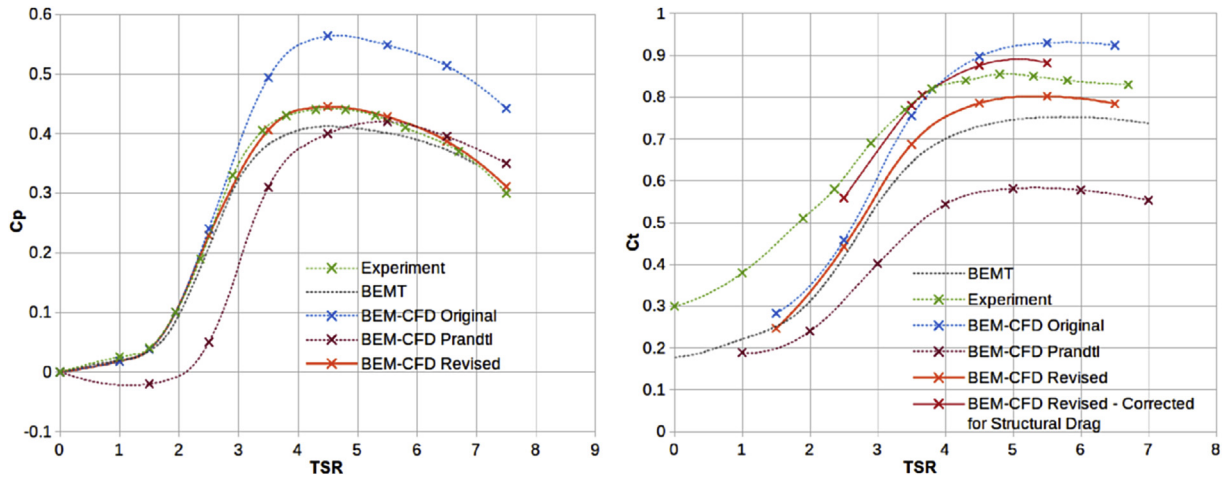
**Fig. 7.** A comparison of predicted $C_P$ and $C_T$ with experimental results for a range of TSR's. Flow speed is 1.2 m/s, and background turbulence intensity is 3%.

particularly in the low TSR range. This is due to the fact that the experimental thrust results are derived from a 6 component load cell located between the assembly mast and rig. As a result of this, the experimental $C_T$ includes the axial force on the whole structure, i.e. the hydrofoils, hub and mast.

Corrected revised BEM-CFD $C_T$ values, calculated using a very simplified representation of the assembly (see Section 2.4.3), are

also presented in Fig. 7 and demonstrate a reasonable correlation with the experimental data. However, the method of approximation is likely subject to error due to over simplification, and thus the values should be treated with the appropriate caution. The BEMT $C_T$ data shows a small under prediction compared to the revised BEM-CFD $C_T$ results, however this is due to the BEMT method not capturing the blockage effects of the flume geometry. The original
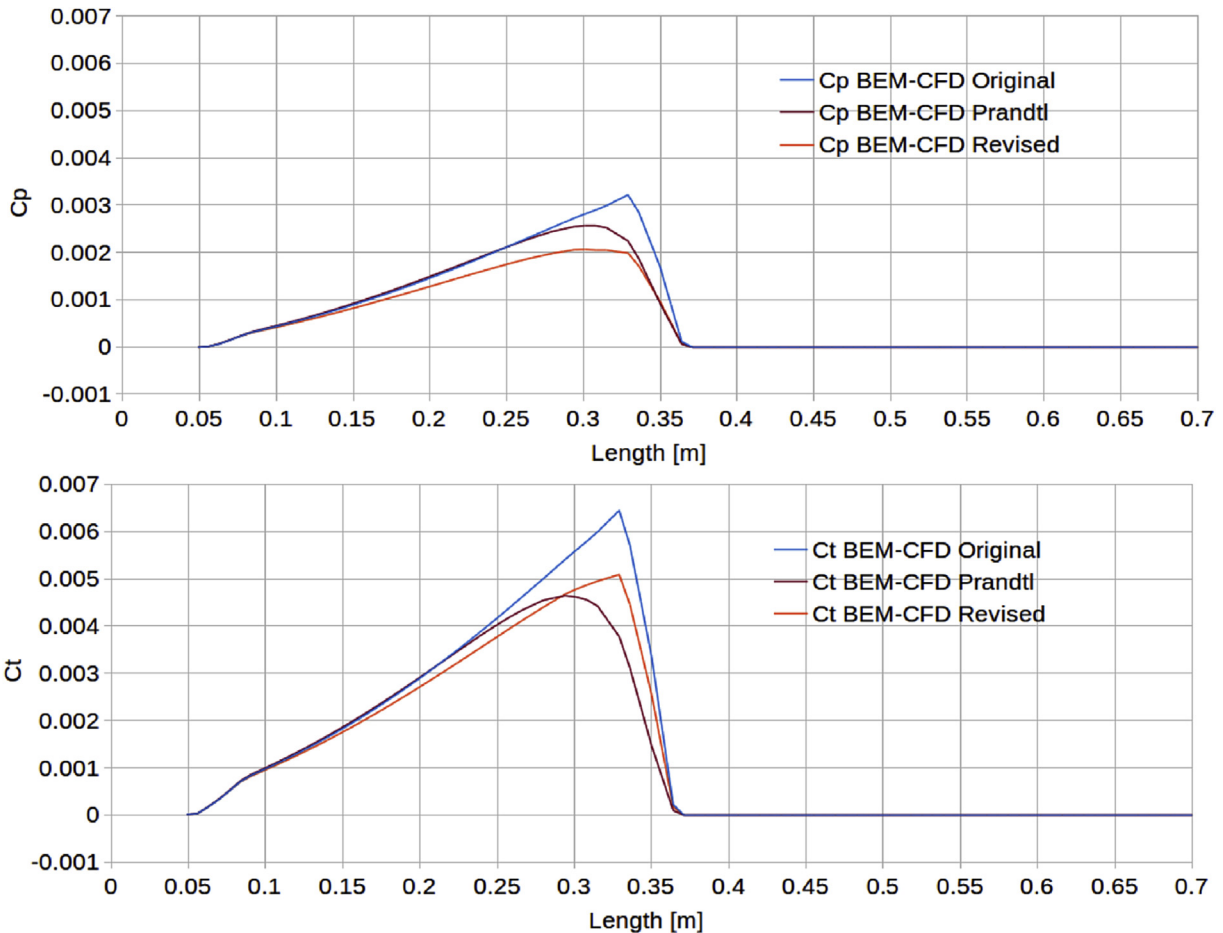


**Fig. 8.** A comparison of the distribution of predicted $dC_P$ and $dC_T$ from rotor centre to hydrofoil tip. The simulations are conducted at a TSR of 3.67, a flow speed of 0.8 m/s, and background turbulence intensity is set at 3%.
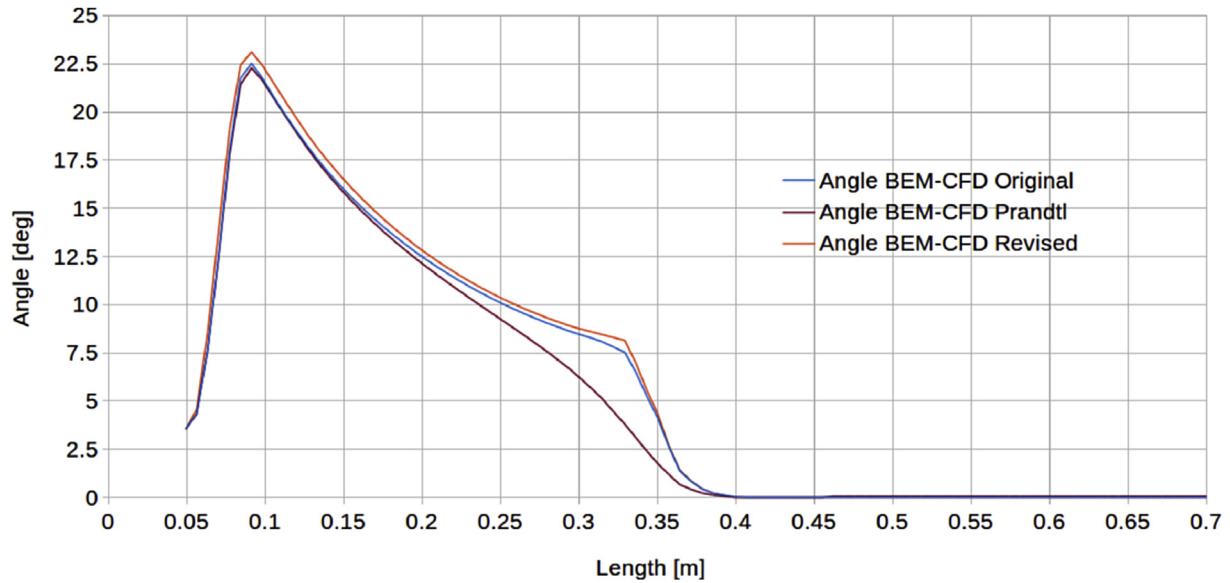
**Fig. 9.** A comparison of the distribution of predicted rotor disk outflow angle, from rotor centre to hydrofoil tip. The simulations are conducted at a TSR of 3.67, a flow speed of 0.8 m/s, and background turbulence intensity is set at 3%.

BEM-CFD $C_T$ data shows a significant over prediction above TSR 2.5 compared to the revised method, while the Prandtl tip loss BEM-CFD $C_T$ data shows a significant under prediction across the whole range.

Fig. 8 shows the distribution of $C_P$ and $C_T$ along a sample line from hub centre to a radial location of 0.7 m for the original, Prandtl tip loss and revised BEM-CFD methods. The distribution trend for the first two thirds of the hydrofoil is similar for the original and Prandtl tip loss BEM-CFD methods, while the last third differs. The distribution for the revised method shows a steadily increasing difference. Both the Prandtl BEM-CFD and the revised BEM-CFD methods show a reduction in $C_P$ and $C_T$ as compared with the original method.

In summary, the revised BEM-CFD method correlates well with the industry recognised BEMT model for both $C_P$ and $C_T$. The observed differences are due to blockage effects, i.e. BEMT does not include a method for capturing their effects on performance. The revised BEM-CFD method also correlates well with the experimental data for both $C_P$ and $C_T$, when the mast and nacelle correction is applied.

### 3.4.2. Comparison of predicted inclination angle, and turbulence

The previous subsection looked at the distribution of $C_P$ and $C_T$ along a sample line from hub centre to a radial location of 0.7 m. This subsection examines the rotor disk outflow angle and the distribution of turbulence intensity along the same sample line. Fig. 9 shows the distribution of disc averaged flow inclination exiting the blade area relative to the rotor disc plane. Both the original and revised BEM-CFD methods have similar trends, with the revised method showing a slight increase in angle of inclination. The Prandtl tip loss method however significantly falls toward zero outflow angle in the last third of the hydrofoil.

Fig. 10 highlights an interesting observation of the distribution of turbulence along the hydrofoil. It can be seen that the Prandtl tip loss method again doesn't follow the same trend as the original and revised BEM-CFD methods. Although initially higher than the original method, the $Ti$ drops off significantly towards the hydrofoil tip. The revised method demonstrates a significant increase in $Ti$ along the hydrofoil, peaking towards the hydrofoil tip region.

Turbulence generation, in part, is a function of the shear stress associated with velocity gradients. Along the hydrofoil, and
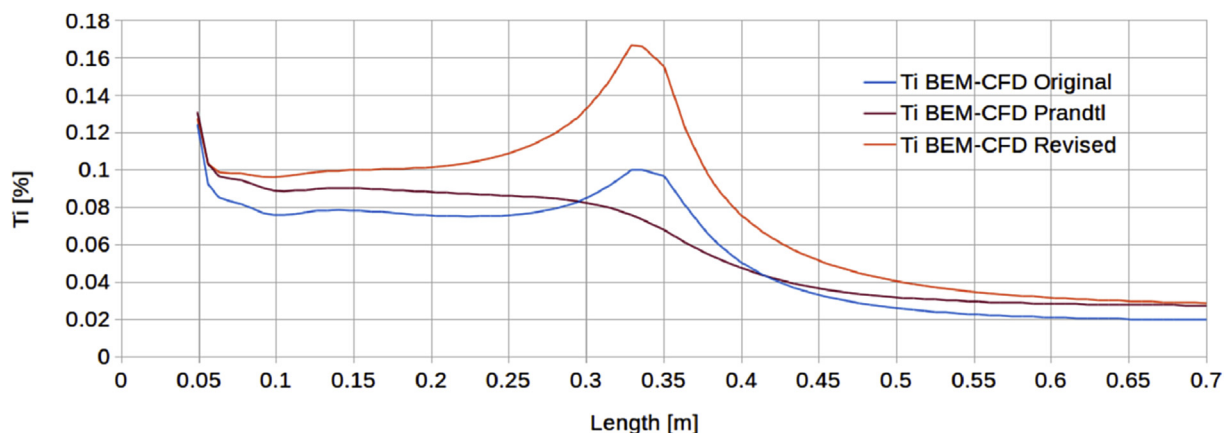


**Fig. 10.** A comparison of the distribution of predicted turbulence intensity $Ti$ from rotor centre to hydrofoil tip. The simulations are conducted at a TSR of 3.67, a flow speed of 0.8 m/s, and background turbulence intensity is set at 3%.

particularly at the tip, there is an increased deflection of the flow with respect to the free stream velocity. This in turn increases the velocity gradient in the region of the hydrofoil, and thus the turbulence generation rate.

### 3.4.3. Observations of the near wake region

The distribution of axial velocity magnitude and turbulence intensity in the region behind the rotor is a time averaged approximation of real flow phenomena. The results in Fig. 11 highlight two main characteristics of interest when comparing the velocity fields. The first is the velocity deficit and second is the wake boundary velocity gradient. The results in Fig. 11 show the velocity deficit in the revised BEM-CFD method is greater than observed in the original and Prandtl tip loss methods. The Prandtl

tip loss method shows the smallest deficit in the near wake region. The rate of change of velocity magnitude at the wake edge is smaller in the Prandtl tip loss method, and greatest in the revised method.

These characteristics support the results observed for the near wake turbulence intensity in Fig. 12. The effects of the turbulence distribution at the rotor plane shown in Fig. 10 can effectively be seen propagating downstream. The increase in turbulence intensity for the revised BEM-CFD method, particularly at the wake boundary, has the effect of improving wake recovery. Figs. 13–15, demonstrate the velocity deficit in the wake from the revised BEM-CFD correlates well, although very symmetric, with the experimental results from Ref. [25]. It can be seen in Fig. 14 the velocity deficit distribution holds well with experiment, the greatest
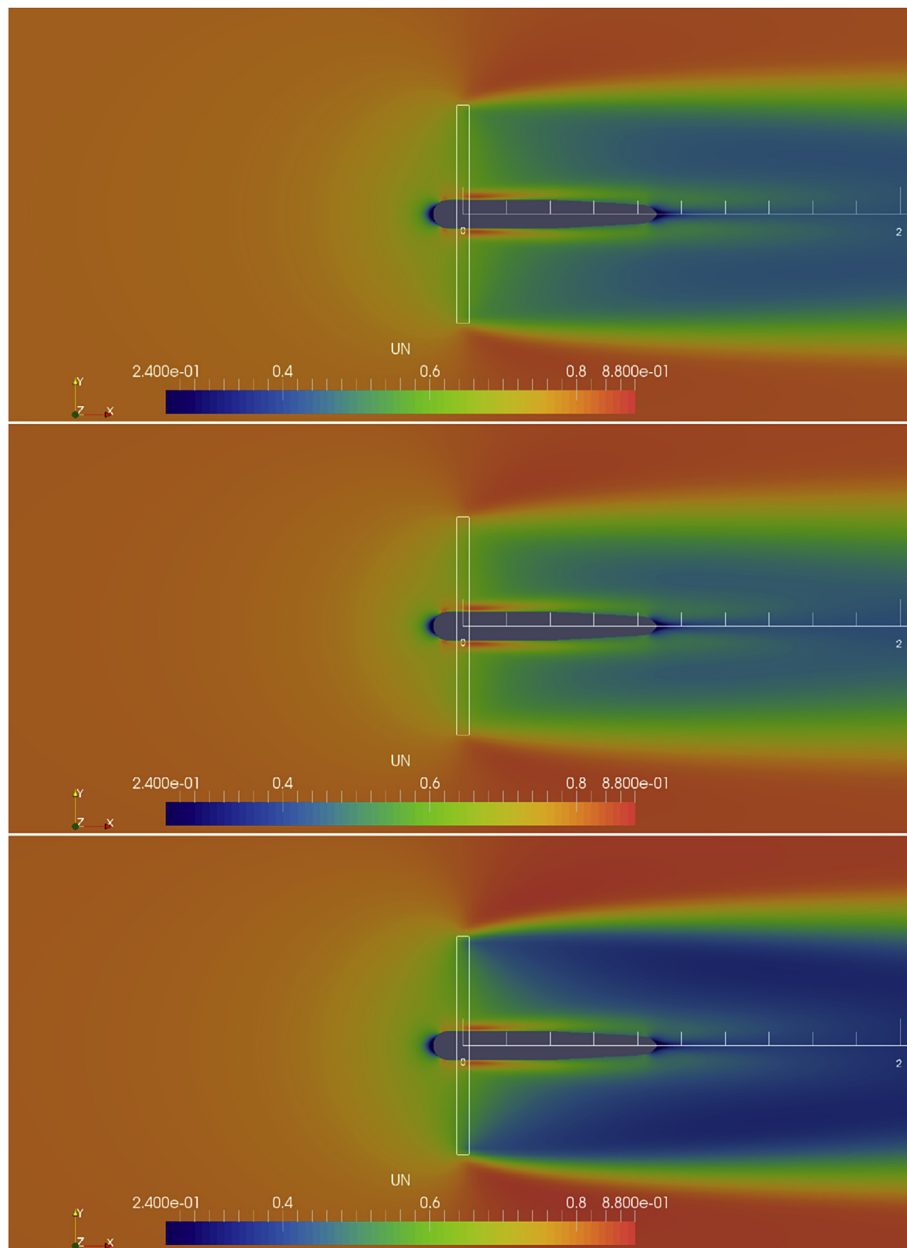


**Fig. 11.** A comparison of the three numerical models studied in this work. Axial velocity (UN) slices taken through the x-y plane at hub height. The rotor disc area is outlined in white at the centre of the images. The simulations are conducted at a TSR of 3.67, a flow speed of 0.8 m/s, and background turbulence intensity is set at 3%. The top images are of the original BEM-CFD model, the middle images are of the BEM-CFD model with Prandtl tip loss factor applied, and the bottom images are of the revised BEM-CFD utilising Prandtl's Lifting Line Theory.
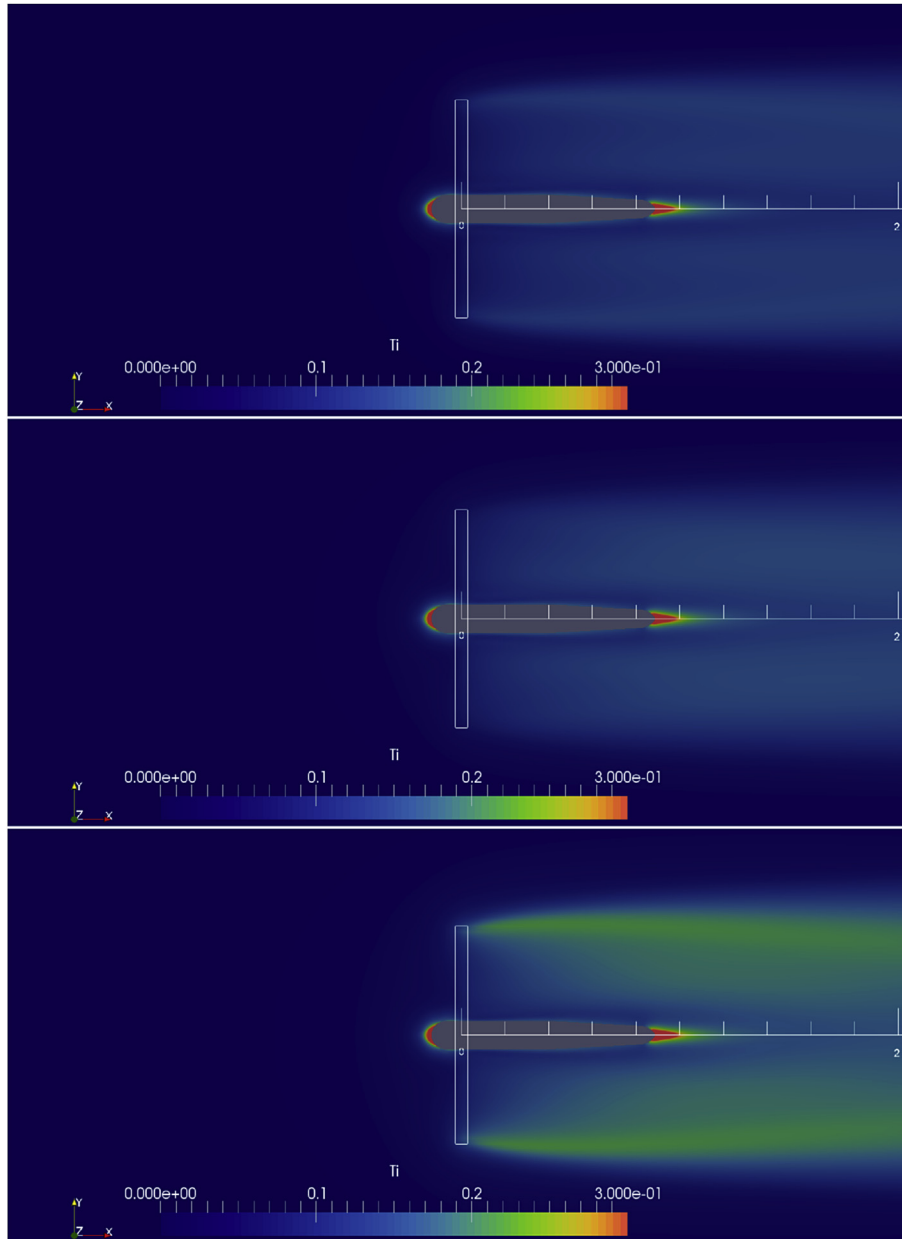
**Fig. 12.** A comparison of the three numerical models studied in this work. Turbulence intensity (Ti) slices taken through the x-y plane at hub height. The rotor disc area is outlined in white at the centre of the images. The simulations are conducted at a TSR of 3.67, a flow speed of 0.8 m/s, and background turbulence intensity is set at 3%. The top images are of the original BEM-CFD model, the middle images are of the BEM-CFD model with Prandtl tip loss factor applied, and the bottom images are of the revised BEM-CFD utilising Prandtl's Lifting Line Theory.

deviation is close to the rotor at 1.2 diameters downstream. The turbulence intensity comparisons in Fig. 15 show similar trends with correlation improving further downstream.

## 4. Conclusions

When compared to the experimental data published by Ref. [25], the revised BEM-CFD method, described in Section 2.2, shows a significant improvement over previous BEM-CFD methods when predicting power and thrust. The revised method also compares favourably with the industry recognised BEMT method. Differences in predictions are accounted for as a result of flow blockage effects captured by the BEM-CFD method.

Comparing the three BEM-CFD methods, a study of the

distribution of $C_P$, $C_T$, wake inclination angle, and turbulence intensity along the radius of the disk averaged hydrofoils was conducted. It is observed that the steady change in distribution along the length of the disk averaged hydrofoils, compared with the original BEM-CFD method, hold with the concept of a steadily changing downwash angle increasing towards the hydrofoil tip. The comparison also demonstrates that the Prandtl tip loss BEM-CFD method doesn't correlate well with observations of experimental results [25]. This is because the Prandtl tip loss BEM-CFD method effectively reduces the momentum extracted from the local flow towards the hydrofoil tip, thus allowing the flow to continue unaffected by the rotor. This significantly reduces the flow inclination exiting the rotor area, and has an additional effect of reducing the velocity gradient at the wake boundary. This in turn affects the
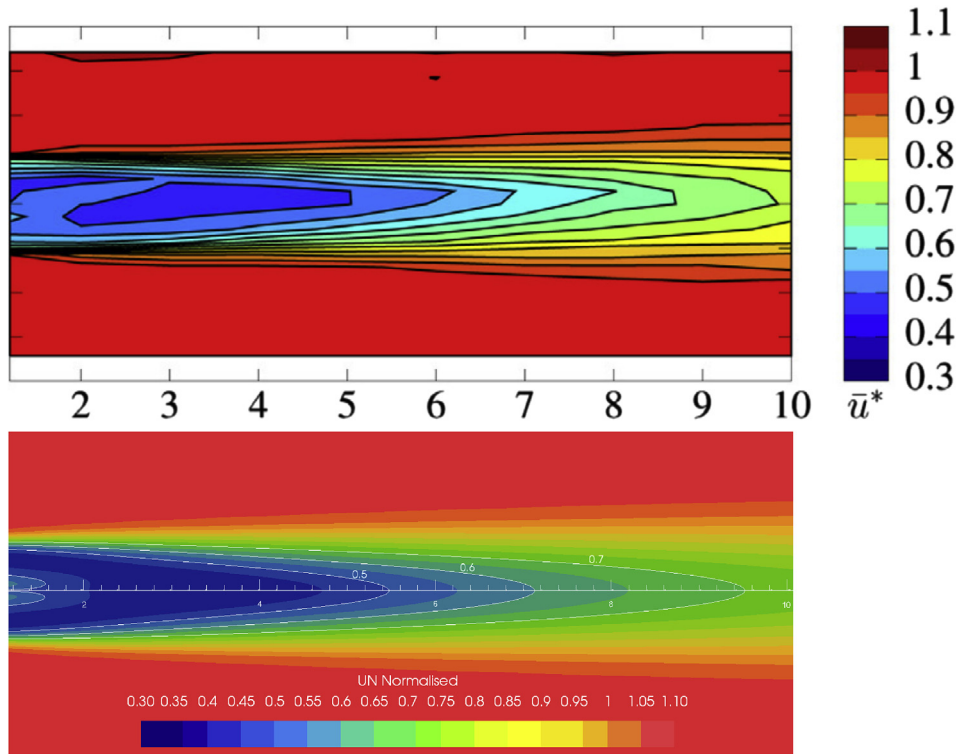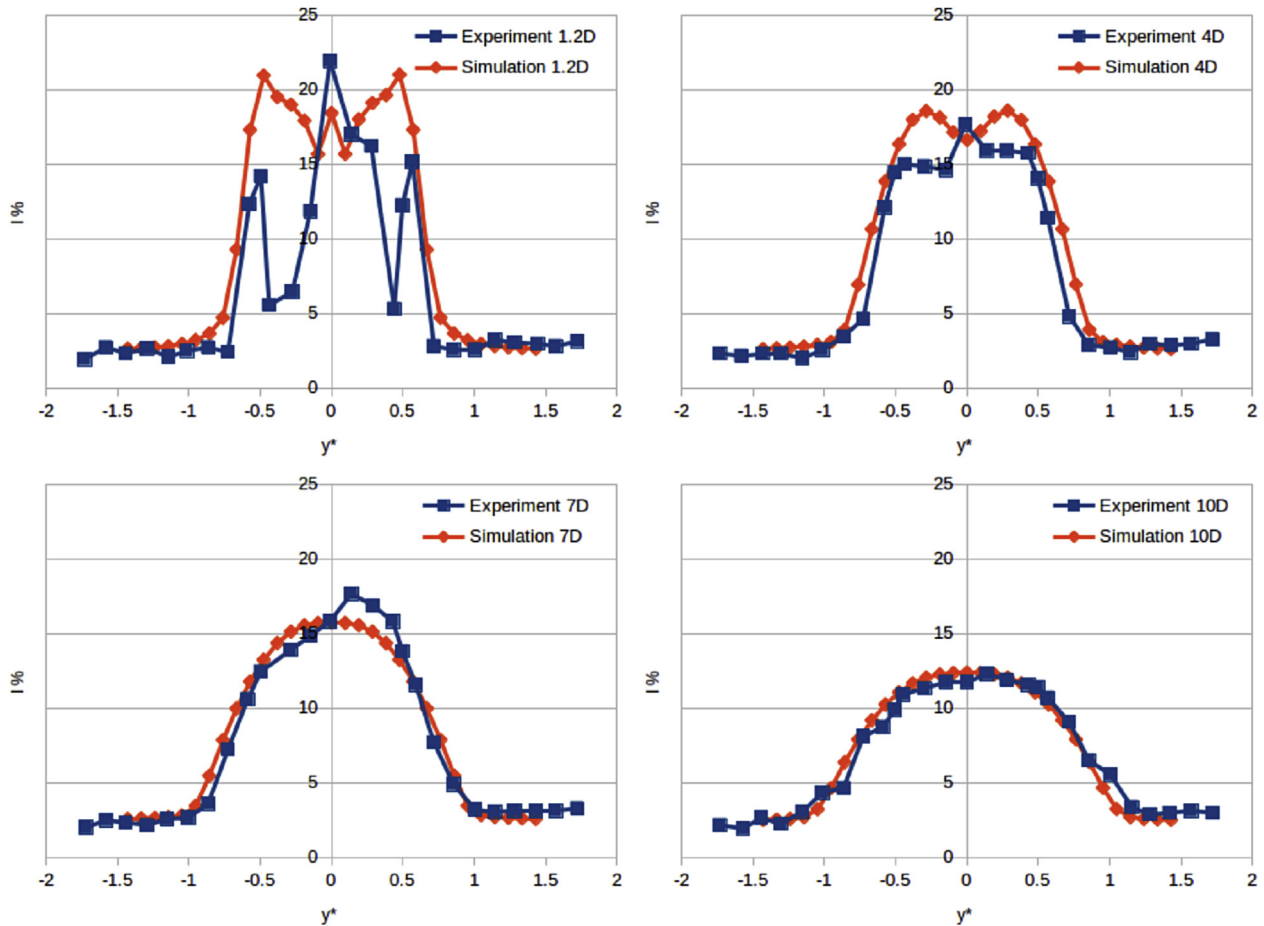
**Fig. 13.** A comparison of numerical and experimental axial velocity slices taken at hub centre. Free stream velocity is 0.8 m/s, TSR is 3.67, and background turbulence intensity is set at 3%. The top visualisation is Fig. 9a from Ref. [25]. Image courtesy of [25] © Renewable Energy. The lower visualisation is staged for direct comparison.
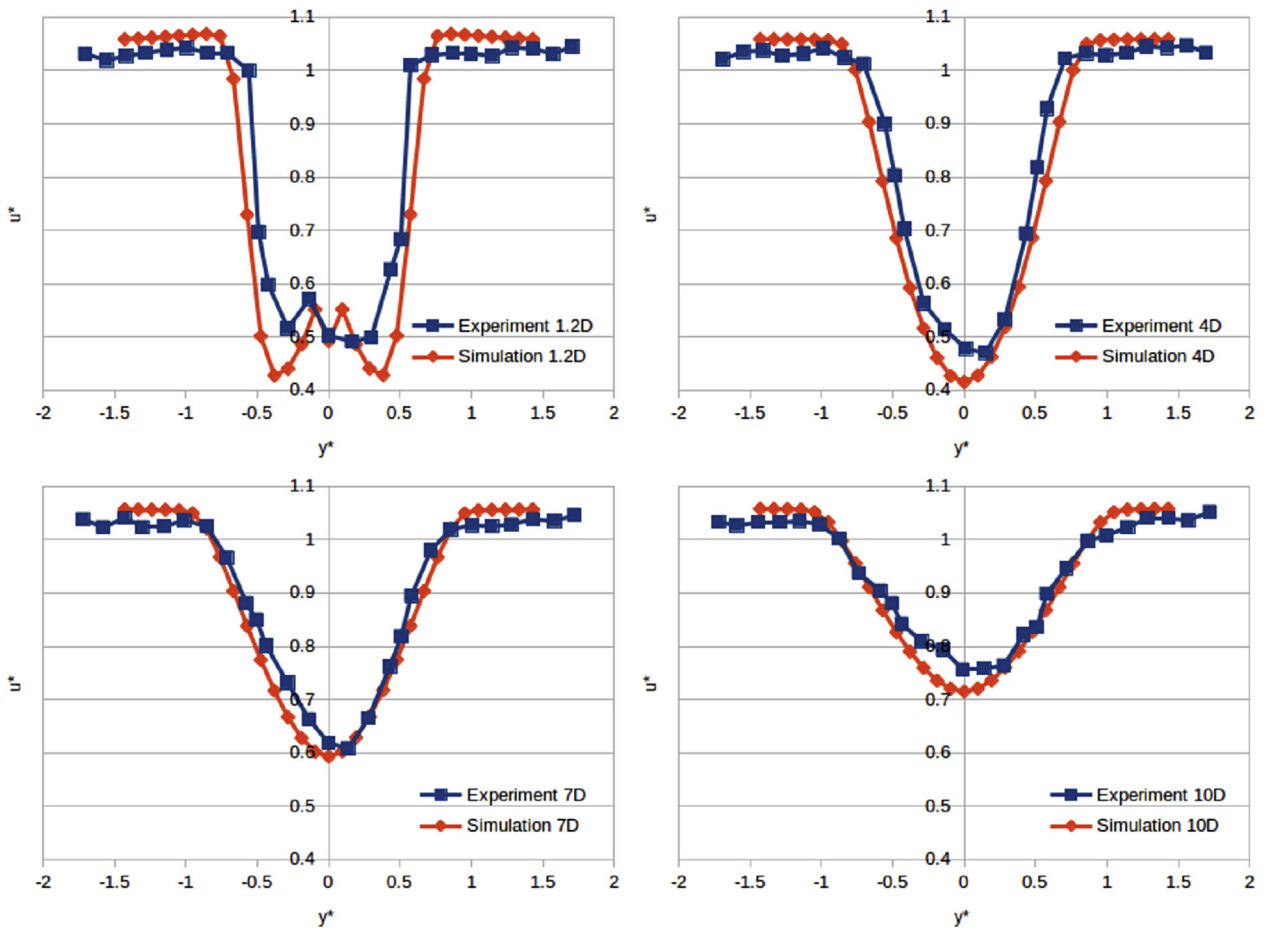


**Fig. 14.** A comparison of numerical and experimental axial velocity transects taken at hub height. Free stream velocity is 0.8 m/s, TSR is 3.67, and background turbulence intensity is set at 3%. The velocity [$u^*$], and width [$y^*$] are normalised by diameter. Each graph compares experimental results with simulation results for a range of diameters downstream [1.2,4.0,7.0,10.0].

**Fig. 15.** A comparison of numerical and experimental turbulence intensity transects taken at hub height. Free stream velocity is 0.8 m/s, TSR is 3.67, and background turbulence intensity is set at 3%. The width $[y^*]$ is normalised by diameter. Each graph compares experimental results with simulation results for a range of diameters downstream [1.2,4.0,7.0,10.0].

quantity of shear generated turbulence at the wake boundary.

In previous work additional source terms are added to increase the wake recovery rate [29]. However this may be unnecessary with the revised BEM-CFD model, due to the consequence/byproduct of increased turbulence generation. The increase in turbulence intensity in the rotor region, in particular at the wake boundary, will increase the rate of momentum transfer into the downstream wake thus improving the recovery without additional empirical turbulence source terms.

In summary, good correlation with experimental results for power, thrust, and wake prediction, is observed using the revised BEM-CFD model. This model also gives good correlation with the industry recognised BEMT method for open hydrofoil horizontal axis tidal turbines.

## 5. Future work

The under prediction observed away from the optimum working range (mainly observed in the thrust curve for this geometry) is likely due to a combination of the simplified lift distribution, i.e. an ellipse, and sensitivity to Reynolds number related lift and drag. A study into methods for better predicting the lift distribution would benefit this research, as would an investigation into the influence of Reynolds number on lift and drag characteristics for a range of TSR and flow speed.

Wake characterisation and sensitivity to turbulence is another

potential topic of further research, which should include the effects of device scaling, and larger than grid scale turbulence modelling. Further investigations into wake recovery in the down stream region with the revised BEM-CFD method, in conjunction with further investigations into which turbulence models best represent this type of simulation method, should be conducted. This includes investigations into the simulation of increased turbulence within a fixed domain such as a flume.

## Acknowledgements

## References

[1] A.S. Bahaj, Marine current energy conversion: the dawn of a new era in

electricity production, Philos. Trans. R. Soc. A Math. Phys. Eng. Sci. 371 (1985) (2013) 20120500.

[2] The Crown Estate, UK Wave and Tidal Key Resource Areas Project, Tech. Rep. Version 2, 12 October 2012, The Crown Estate, October 2012, http://www.thecrownestate.co.uk/.

[3] J. Whelan, J. Graham, J. Peiro, A free-surface and blockage correction for tidal turbines, J. Fluid Mech. 624 (2009) 281–291.

[4] T. Nishino, R.H. Willden, Two-scale dynamics of flow past a partial cross-stream array of tidal turbines, J. Fluid Mech. 730 (2013) 220–244.

[5] S. Draper, T. Nishino, Centred and staggered arrangements of tidal turbines, J. Fluid Mech. 739 (2014) 72–93.

[6] R. Von Mises, Theory of Flight, No. 1 in Dover Books on Aeronautical Engineering Series, Dover Publications, 1959. http://books.google.co.uk/books?id=H_O45Qy-ngwC.

[7] R. Griffiths, M. Woollard, Performance of the optimal wind turbine, Appl. Energy 4 (4) (1978) 261–272.

[8] T. Burton, N. Jenkins, D. Sharpe, E. Bossanyi, Wind Energy Handbook, John Wiley & Sons, 2011.

[9] J. Chapman, I. Masters, M. Togneri, J. Orme, The buhl correction factor applied to high induction conditions for tidal stream turbines, Renew. Energy 60 (2013) 472–480, http://dx.doi.org/10.1016/j.renene.2013.05.018. http://www.sciencedirect.com/science/article/pii/S0960148113002632.

[10] A. Mason-Jones, D.M. O'Doherty, C.E. Morris, T. O'Doherty, C. Byrne, P.W. Prickett, R.I. Grosvenor, I. Owen, S. Tedds, R. Poole, Non-dimensional scaling of tidal stream turbines, Energy 44 (1) (2012) 820–829.

[11] J. McNaughton, S. Rolfo, D. Apsley, T. Stallard, P. Stansby, CFD power and load prediction on a 1MW tidal stream turbine with typical velocity profiles from the EMEC test site, in: Proceedings of the 10th European Wave and Tidal Energy Conference. 2nd–5th September, Aalborg, 2013.

[12] M. Willis, I. Masters, S. Thomas, R. Gallie, J. Loman, A. Cook, R. Ahmadian, R. Falconer, B. Lin, G. Gao, et al., Tidal turbine deployment in the bristol channel: a case study, Proc. ICE-Energy 163 (3) (2010) 93–105.

[13] M. Harrison, W. Batten, A. Bahaj, A blade element actuator disc approach applied to tidal stream turbines, OCEANS 2010 (2010) 1–8.

[14] R. Malki, A. Williams, T. Croft, M. Togneri, I. Masters, A coupled blade element momentum–computational fluid dynamics model for evaluating tidal stream turbine performance, Appl. Math. Model. 37 (5) (2013) 3006–3020.

[15] L. Lavaroni, S.J. Watson, M.J. Cook, M.R. Dubal, A comparison of actuator disc and BEM models in CFD simulations for the prediction of offshore wake losses, J. Phys. Conf. Ser. 524 (2014) 012148. IOP Publishing.

[16] Q. Guo, L. Zhou, Z. Wang, Comparison of bem-cfd and full rotor geometry simulations for the performance and flow field of a marine current turbine, Renew. Energy 75 (2015) 640–648.

[17] A. Bahaj, A. Molland, J. Chaplin, W. Batten, Power and thrust measurements of marine current turbines under various hydrodynamic flow conditions in a cavitation tunnel and a towing tank, Renew. energy 32 (3) (2007) 407–426.

[18] PHYSICA, A Multi-Physics Computational Fluid Dynamics and Computational Solid Mechanics Framework, http://staffweb.cms.gre.ac.uk/˜physica/, Retrieved: July 2015.

[19] N. Croft, K. Pericleous, M. Cross, Physica: a Multiphysics Environment for Complex Flow Processes, Numerical Methods in Laminar and Turbulent Flow 9 (Pt 2), 1995, pp. 1269–1280.

[20] H.G. Weller, G. Tabor, H. Jasak, C. Fureby, A tensorial approach to computational continuum mechanics using object-oriented techniques, Comput. Phys. 12 (6) (1998) 620–631.

[21] B. Launder, D. Spalding, Mathematical Models of Turbulence, Academic Press, London, 1972.

[22] V. Yakhot, S. Orszag, S. Thangam, T. Gatski, C. Speziale, Development of turbulence models for shear flows by a double expansion technique, Phys. Fluids A Fluid Dyn. (1989–1993) 4 (7) (1992) 1510–1520.

[23] I. Abbott, A. Von Doenhoff, Theory of Wing Sections, Including a Summary of Airfoil Data, No. 1 in Dover Books on Aeronautical Engineering Series, Dover Publications, 1959. http://books.google.co.uk/books?id=DPZYUGNyuboC.

[24] J. Anderson, Fundamentals of Aerodynamics, No. 5 in Anderson Series, McGraw-Hill Education, 2010. http://books.google.co.uk/books?id=xwY8PgAACAAJ.

[25] P. Mycek, B. Gaurier, G. Germain, G. Pinon, E. Rivoalen, Experimental study of the turbulence intensity effects on marine current turbines behaviour. Part i: one single turbine, Renew. Energy 66 (2014) 729–746.

[26] F. Maganga, G. Germain, J. King, G. Pinon, E. Rivoalen, Experimental characterisation of flow effects on marine current turbine behaviour and on its wake properties, IET Renew. Power Gener. 4 (6) (2010) 498–509.

[27] T. ODoherty, A. Mason-Jones, D.M. ODoherty, P.S. Evans, C. Wooldridge, I. Fryett, Considerations of a horizontal axis tidal turbine, Proc. ICE-Energy 163 (3) (2010) 119–130.

[28] M. Edmunds, R. Malki, A. Williams, I. Masters, T. Croft, Aspects of tidal stream turbine modelling in the natural environment using a coupled bemcfd model, Int. J. Mar. Energy 7 (2014) 20–42.

[29] S.R. Turnock, A.B. Phillips, J. Banks, R. Nicholls-Lee, Modelling tidal current turbine wakes using a coupled RANS-BEMT approach as a tool for analysing power capture of arrays of turbines, Ocean. Eng. 38 (11) (2011) 1300–1307.